

TABLE 1 Comparison of Resonant Frequencies of First Three Modes of Rectangular Cavity Using Conventional ADI FDTD (C_ADI) and Anisotropic ADI FDTD (A_ADI)

Cell Dimension	Analytical [12]	Courant Stability Factor (S)			
		4		8	
		C_ADI	A_ADI	C_ADI	A_ADI
$\Delta x = \Delta z = \delta_1$ $\Delta y = \delta_2$	9.2723	9.2396	9.2801	9.1507	9.2922
	14.662	14.575	14.687	14.395	14.631
	16.145	16.013	16.129	15.923	16.208
$\Delta x = \Delta z = 2*\delta_1$ $\Delta y = \delta_2$	9.2723	9.2066	9.2895	9.0623	9.293
	14.662	14.425	14.475	14.268	14.360
	16.145	15.986	16.101	15.859	16.236

$\delta_1 = 0.5715$ mm; $\delta_2 = 0.5644$ mm.

0.35% with $S = 4$ and for A_ADI_FDTD, error is 0.21% with $S = 8$. This indicates that for similar accuracy, CPU time can be saved by the factor of 2 because the total number of sample collected for $S = 4$ is 1024 and for $S = 8$ is 512. It is being noticed from several iteration that A_ADI_FDTD saves 2.5–3 times of CPU time over the C_ADI_FDTD to achieve the same level of accuracy. Comparison of CPU time and accuracy for conventional ADI FDTD and standard FDTD is discussed in details in [2] and it is found out that for the similar accuracy, conventional ADI FDTD is 1.6 times faster than standard FDTD [2]. Hence the A_ADI_FDTD is overall four to five times faster than standard FDTD for same level of accuracy. Table 1 also shows the improvement of A_ADI_FDTD for larger cell dimensions.

5. CONCLUSION

The accurate numerical dispersion expression is provided for artificial anisotropic ADI FDTD for three-dimensional case. The optimum values of anisotropic parameters have been calculated using the accurate numerical dispersion relation. It is shown that anisotropic ADI FDTD always reduces error as compared with conventional ADI FDTD for any value of mesh resolution, courant number, and cell dimension ratio. Anisotropic ADI FDTD also provides the better accuracy with identical CPU time or lesser CPU time for same accuracy over the conventional ADI FDTD and standard FDTD.

REFERENCES

1. T. Namiki, A new FDTD algorithm based on alternating -direction implicit method, IEEE Trans Microwave Theory Tech MTT-47 (1999), 2003-2007.
2. F. Zheng, Z. Chen, and J. Zhang, Toward the development of a three-dimensional unconditionally stable finite difference time domain method, IEEE Trans Microwave Theory Tech MTT-48 (2000), 1550-1558.
3. A. Taflove and S. Hagness, Computational electrodynamics: The finite difference time domain method, 2nd ed., Artech House, Boston, MA, 2000.
4. F. Zheng and Z. Chen, Numerical dispersion analysis of the unconditionally stable 3-D ADI-FDTD method, IEEE Trans Microwave Theory Tech MTT-49 (2001), 1006-1009.
5. A.P. Zhao, The influence of the time step on the numerical dispersion error of an unconditionally stable 3-D ADI-FDTD method: A simple and unified approach to determine the maximum allowable time step required by a desired numerical dispersion accuracy, Microwave Opt Technol Lett 35 (2002), 60-65.
6. M.K. Sun and W.Y. Tam, An unconditionally stable high-order 2-D ADI FDTD method, IEEE Antenna Propag Soc Int Symp Dig 1 (2003), 352-355.
7. S. Ju, K.Y. Jung, and H. Kim, Investigation on the characteristics of

the envelope FDTD based on the alternating direction implicit scheme, IEEE Microwave Wireless Compon Lett 13 (2003), 414-416.

8. S. Wang and F.L. Teixeira, A three-dimensional angle-optimized finite difference time domain algorithm, IEEE Trans Microwave Theory Tech MTT-51 (2003), 811-817.
9. A.P. Zhao, Improvement on the numerical dispersion of 2-D ADI-FDTD with artificial anisotropy, IEEE Microwave Wireless Compon Lett 14 (2004), 292-294.
10. H.X. Zheng and K.W. Leung, An efficient method to reduce the numerical dispersion in the ADI-FDTD, IEEE Trans Microwave Theory Tech MTT-53 (2005), 2295-2301.
11. J.S. Juntunen and T.D. Tsiboukis, Reduction of numerical dispersion in FDTD method through artificial anisotropy, IEEE Trans Microwave Theory Tech MTT-48 (2000), 582-588.
12. S. Dey and R. Mittra, Efficient computation of resonant frequencies and quality factors of cavities via a combination of finite-difference time-domain technique and Pade approximation, IEEE Microwave Wireless Compon Lett 8 (1998), 415-417.
13. K.V. Srivastava, V.V. Mishra, and A. Biswas, An efficient FDTD algorithm for computation of resonance frequencies of an inhomogeneous cylindrical structure, In Asia Pacific Microwave Conference, Japan, December 2006.

© 2007 Wiley Periodicals, Inc.

FAST ALL MODES (FAM) METHOD COMBINED WITH NMSP FOR EVALUATING SPATIAL DOMAIN LAYERED MEDIUM GREEN'S FUNCTIONS OF MODERATE THICKNESS

Boping Wu,¹ Leung Tsang,¹ and Chong-Jin Ong²

¹ Department of Electrical Engineering, University of Washington, Paul Allen Center—Room AE100R, Campus Box 352500, Seattle, WA 98195-2500; Corresponding author: bennywu@u.washington.edu

² Memory Products Group, Micron Technology, Inc., 8000 South Federal Way, Post Office Box 6, Boise, ID 83707-0006

Received 10 May 2007

ABSTRACT: An efficient and novel approach, the fast all modes (FAM) method, was developed to locate all modes precisely on the entire complex plane for a single layered media. The modes include surface wave modes, leaky wave modes, and improper modes. For the case where the layer thickness is 1 wavelength, the pre-processing FAM requires 0.34 s for computing 500 mode locations of both TE and TM modes using a Pentium IV 3.2 GHz PC running Matlab. To justify our FAM method, we use the numerical modified steepest-descent path

(NMSP) method to evaluate spatial domain Green's functions for mixed potentials G_A and G_V . The NMSP method computes the steepest descent integral with all the pole proximities extracted and replaced by incomplete error functions. The CPU per distance point based on the FAM/NMSP method takes less than 6 mss for all distance ranges. All computed results are accurate to within 0.2% of the conventional half space extraction method. © 2007 Wiley Periodicals, Inc. Microwave Opt Technol Lett 49: 3112–3118, 2007; Published online in Wiley InterScience (www.interscience.wiley.com). DOI 10.1002/mop.22907

Key words: Green's functions; layered media; leaky wave modes; improper modes; fast all modes method

1. INTRODUCTION

The evaluation of layered medium Green's functions is necessary when using method of moment (MoM) for full wave analysis in antenna design, high speed circuit modeling and wireless communication simulation. It is well known that the conventional Sommerfeld integration path (SIP) representation of layered medium Green's function is very poorly convergent, because of the highly oscillatory behavior of the integrands along the SIP. Some alternative methods using a deformed path from the SIP, such as discrete complex image method (DCIM), have been developed [1, 2]. However, for moderate or large separation between the source and field point, the error in selecting the optimal path for the space-independent part will be magnified when integrated with the space-dependent part.

In our recent research, we used the numerical modified steepest-descent path (NMSP) method to calculate the electromagnetic fields of Hertzian dipoles (layered medium Green's functions) for both thin layers [3] and layers of moderate thickness [4] at all distance range. The NMSP method can integrate along the steepest descent path (SDP) efficiently using the least CPU and only a few integration points after the extraction of all the singularity poles nearby. This is because, (1) the SDP can minimize or eliminate the fast oscillation of the space-dependent Hankel functions inside the integrand, (2) the integrand on SDP decays exponentially at infinity even when both source and field points are on the boundary, and (3) the space-independent part of the integrand is made smooth by extracting all the poles. To perform NMSP efficiently and with good accuracy, it is highly desirable to find all the locations of the corresponding proper and improper modes precisely on the whole complex plane within an acceptable CPU time.

In the past, different numerical iterative approaches of locating modes in layered medium have been investigated by several researchers, including Guglielmi and Jackson [5], Hsu et al. [6], Marin et al. [7], Neve and Paknys [8], and Wang et al. [9]. However, the traditional and approximated initial values will make the iterative scheme converge poorly or even miss out some poles. So far, these methods could only locate a few poles and they cost lots of CPU time for convergence checking.

The purpose of this article is to present our FAM algorithm, which can efficiently determine all mode locations precisely in the complex plane, including surface wave modes, leaky wave modes and improper modes. In this article, we will justify this method by evaluating spatial domain Green's functions for mixed potentials G_A and G_V in a single layered media of moderate thickness (see Fig. 1). For the case where the layer thickness is 1 wavelength, our FAM requires only 0.34 s to determine 500 locations of both transverse electric (TE) and transverse magnetic (TM) modes accurately in the complex plane using a Pentium IV 3.2 GHz PC running Matlab. The Green's functions are then computed by summing the residues of surface wave modes and leaky wave modes together with the contribution of the SDP. Before evaluat-

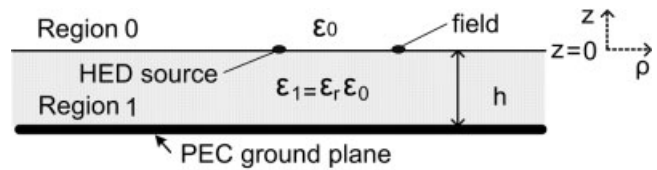


Figure 1 Single layered medium with a HED source at the surface of the dielectric substrate

ing the SDP contribution by the NMSP, all the modes, including the surface wave modes, leaky wave modes, and improper modes, which are close to the saddle point are extracted (see Fig. 2). The pole proximities are accounted for by using incomplete error functions [10]. A trapezoidal integration using less than 50 points is chosen to calculate the SDP contribution. We apply the NMSP/FAM methods to compute the layered medium Green's functions with distances ρ larger than 0.05 wavelengths from the dipole. For the near field with ρ less than 0.05 wavelengths, the Green's functions can be computed by the modified half space extraction method with Gauss-Hermite integration along the vertical branch cuts. The CPU per point is less than 6 ms for the entire distance range. The CPU is significantly faster than those reported using the DCIM [2]. All computed results are within 0.2% accuracy from that computed by the conventional half space extraction method [11]. Unlike the DCIM, the NMSP/FAM method proposed in this article does not need parameter adjustment for different distance ranges. Without benchmark results from the half space methods, our NMSP/FAM can still ensure accuracy by self-convergence checks, for example, by including more residue poles and more integration points. We tabulate the CPU per distance point, the number of leaky wave modes, the number of modes for extraction and the number of points for trapezoidal integration as a function of distance. Results of both G_A and G_V with layer thicknesses equal to 1 wavelength are illustrated in the end of this article.

2. METHODOLOGY

2.1 Evaluation of G_A and G_V in the Spatial Domain

The spatial domain Green's functions for mixed potentials, G_A and G_V , with both horizontal source and field point on the surface ($z = z \ll 0$) of the dielectric substrates are expressed by

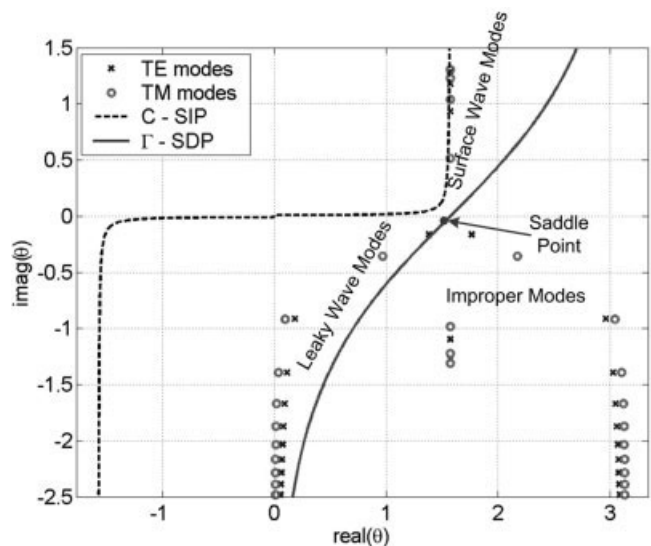


Figure 2 SIP, SDP and TE and TM mode locations on complex θ plane for $h = \lambda$

$$G_A(\rho) = -\frac{j\mu_0}{4\pi} \int_{\text{SIP}} dk_\rho \frac{k_\rho}{k_{0z}} J_0(k_\rho \rho) (1 + R^{\text{TE}}) \quad (1)$$

$$G_V(\rho) = -\frac{j}{4\pi\epsilon_0} \int_{\text{SIP}} dk_\rho \frac{1}{k_{0z}} \left(k_\rho + \frac{k_0^2 R^{\text{TE}} + k_{0z}^2 R^{\text{TM}}}{k_\rho} \right) J_0(k_\rho \rho) \quad (2)$$

where $k_0 = 2\pi/\lambda_0$, ρ and ρ is the source-to-field distance horizontal plane. The electric field at the field point is observed horizontally. R^{TE} and R^{TM} are the reflection coefficients for the TE and TM wave respectively, whose formulations are shown in [11].

2.2 Fast All Modes (FAM) Determination in the Complex Plane

Our FAM method can locate every proper and improper mode on the whole complex plane. We have already presented this idea in a previous article [4] for the TM wave. Here, we will present two complementary methods for TE wave, since both G_A and G_V have lots of modes from the TE wave.

By setting the denominator of the integrand of G_A as zero, we get the mode Eq. (3), whose complex roots containing all modes including surface wave modes, leaky wave modes and improper modes.

$$jk_{0z}h \sin(k_{1z}h) + k_{1z}h \cos(k_{1z}h) = 0 \quad (3)$$

Let $u = k_{1z}h$ and $v = jk_{0z}h$. Then we have the simultaneous equations for the two unknowns u and v .

$$\{f(u,v) = v \sin u + u \cos u = 0 \quad (4)$$

$$\{u^2 = r^2 - v^2 \quad (5)$$

where

$$r^2 = (k_1^2 - k_0^2)h^2$$

2.2.1 Method I—Modes for Small and Moderate Values of v
 $uf(u,v)$ is an even function of u . Using this property of uf , we can transform Eq. (4) into a polynomial equation of v by substituting the Eq. (5) back into it. For example, we use Taylor expansions to expand the Eq. (4).

$$\cos u = \sum_{n=0}^{\infty} c_n u^{2n} \quad (6)$$

and

$$\sin u = \sum_{n=0}^{\infty} s_n u^{2n+1} \quad (7)$$

where

$$s_n = (-1)^n / (2n + 1)$$

and

$$c_n = (-1)^n / (2n)$$

After replacing the unknown u with v using Eqs. (6) and (7), we truncate the Taylor series at $N_{\text{max}} + 1$, and exchange orders of summations. Finally we have the polynomial equation in v as follows.

$$\sum_{k=1}^{N_{\text{max}}+1} v^{2k+1} \sum_{n=k-1}^{N_{\text{max}}} s_n (-1)^k \binom{n+1}{k} r^{2(n+1-k)} + \sum_{k=1}^{N_{\text{max}}+1} v^{2k} \sum_{n=k-1}^{N_{\text{max}}} c_n (-1)^k \binom{n+1}{k} r^{2(n+1-k)} + v \sum_{n=0}^{N_{\text{max}}} s_n r^{2(n+1)} + \sum_{n=0}^{N_{\text{max}}} c_n r^{2(n+1)} = 0 \quad (8)$$

Equation (8) is a polynomial equation of v of the order $v^{2N_{\text{max}} + 3}$. Let the absolute value of the largest root obtained from this Taylor expansion method be v_{max} . We set the appropriate value for N_{max} such that $v_{\text{max}}^2 > r^2$, in order to ensure that all the surface wave modes are found.

Since this Taylor expression is valid for the whole complex plane, all modes for small and moderate values of v in the complex plane can be found by solving the Eq. (8). Among them, roots with pure positive real parts are surface wave modes; roots with positive imaginary parts are leaky wave modes; and the rest are improper modes. (Table 1 column 4 and 5 and Fig. 2.)

TABLE 1 Roots of the Polynomial Equations From Taylor Expansion

Mode Index	Method I for TM Mode, $N_{\text{max}} = 30$		Method I for TE Mode, $N_{\text{max}} = 30$	
	v	θ	v	θ
1	3.3844	1.5708 + 0.5155j	-1.0041 - 1.2051j	1.7613 - 0.1620j
2	-1.8919 - 3.7845j	2.1722 - 0.3575j	-1.0041 + 1.2051j	1.3803 - 0.1620j
3	-1.8919 + 3.7845j	0.9694 - 0.3575j	6.7649	1.5708 + 0.9346j
4	-7.2371	1.5708 - 0.9848j	-8.3500	1.5708 - 1.0960j
5	7.7758	1.5708 + 1.0398j	-1.1815 - 8.9382j	2.9606 - 0.9126j
6	-9.7494	1.5708 - 1.2231j	-1.1815 + 8.9382j	0.1810 - 0.9126j
7	-10.7633	1.5708 - 1.3074j	9.2529	1.5708 + 1.1795j
8	-0.6412 - 9.0668j	3.0442 - 0.9162j	-10.3162	1.5708 - 1.2710j
9	-0.6412 + 9.0668j	0.0974 - 0.9162j	10.4964	1.5708 + 1.2858j
10	9.8645	1.5708 + 1.2330j	-1.3340 - 13.3476j	3.0290 - 1.3931j
11	10.7740	1.5708 + 1.3083j	-1.3340 + 13.3476j	0.1126 - 1.3931j
12	-0.4291 - 13.4294j	3.1055 - 1.3936j	-1.4676 - 17.2114j	3.0503 - 1.6702j
13	-0.4291 + 13.4294j	0.0361 - 1.3936j	-1.4676 + 17.2114j	0.0913 - 1.6702j
14	-0.3598 - 17.2821j	3.1192 - 1.6704j	-1.5863 - 20.8350j	3.0619 - 1.8717j
15	-0.3598 + 17.2821j	0.0223 - 1.6704j	-1.5863 + 20.8350j	0.0797 - 1.8717j

2.2.2 Method II—Modes for Large Values of v and u
 For large values of v and u ,

$$v \approx -ju[1 - r^2/(2u^2)] \quad (9)$$

Substituting into the mode equation, we then have a rough initial guess from first order approximation

$$p_0 = j(m + 1/2)\pi \quad (10)$$

where

$$u_0 = -jp_0$$

and

$$m = 0, 1, 2, 3, \dots$$

A more accurate value is provided by

$$v = -p[1 + r^2/(2p^2)] \quad (11)$$

where

$$p = p_0 + \tan^{-1}[1 + r^2/(2p_0^2)]$$

With this supplementary method for large v and u , all modes on the whole complex plane can be found instantaneously.

In order not to duplicate modes obtained from method I, we only accept those $v > v_{\max}$ in the large v and u method. The larger roots are with complex conjugate pairs of v . Among them, half of the roots with positive imaginary parts are leaky wave modes and the rest (the complex conjugates) are improper modes.

2.2.3 Test and Refinement of the Roots

To verify the roots, we can substitute them back into Eq. (4) to check whether Eq. (4) is satisfied. Those that satisfy Eq. (4) will be kept for refinement by the Newton-Raphson method. The roots $v^{(0)}$ generated by these two complementary methods will be used as initial values for refinement iteration. $u^{(0)}$ can also be calculated by $u^{(0)} = \sqrt{r^2 - (v^{(0)})^2}$. The refinement iteration equation is shown as follows.

$$u^{(n+1)} = u^{(n)} - f(u^{(n)})/(df/du)_{u=u^{(n)}} \quad (12)$$

We terminate the iteration by the following accuracy criteria.

$$\left| \frac{f(u^{(n)})}{u^{(n)}(df/du)_{u=u^{(n)}}} \right| \leq 10^{-6} \quad (13)$$

In this article, we illustrate the results for $\mu_1 = \mu_0$. For the case $h = 1$ wavelength and TE wave only, the determination of all accurate locations up to 250 TE modes on the whole complex plane using method I plus method II requires CPU time of 0.13 s. Because of the exact locations of the roots generated from the above two complementary methods, the refinement using Newton-Raphson method converges very quickly and only takes less than four iterations to meet the accuracy criteria. We can also confirm that all the surface wave modes have been found by the following mode volume formula (Table 2 column 2 and 3).

$$r/\pi < N_s < r/\pi + 1 \text{ for TM modes}$$

$$r/\pi - 0.5 < N_s < r/\pi + 0.5 \text{ for TE modes}$$

This FAM calculation needs only to be computed once as the pre-processing and modes found can be used for all field locations.

2.3 NMSP Method Including Effects of All Modes for Non-Near Field $\rho > 0.05 \lambda$

Using $k_\rho = k_0 \sin \theta$ and $k_{oz} = k_0 \cos \theta$, we can map the complex k_ρ plane to the complex θ plane. We labeled the SIP as C . The SDP labeled Γ is defined by $\text{Re}(\sin \theta) = 1$ (see Fig. 2).

Our method consists of integration along Γ and evaluation of the residues from all proper modes, including the surface wave modes and leaky wave modes, which are located between C and Γ .

$$G_A = G_A^\Gamma - 2\pi j \sum_p R_{k_{pp}} \quad (14)$$

where G_A^Γ is the integration along the steepest descent path Γ ; and $R_{k_{pp}}$ is the residue of mode p between C and Γ from the TE wave. The expression here for G_V is almost the same, except part of the modes for G_V are from the TM wave.

The following is the calculation of the residues for G_A

$$R_{k_{pp}} = H_0^{(2)}(k_{pp}\rho) N(k_{pp})/[dD(k_\rho)/dk_\rho]_{k_\rho=k_{pp}} \quad (15)$$

where

$$N(k_{pp}) = 2j \sin(u) k_{pp} h$$

$$[dD(k_\rho)/dk_\rho]_{k_\rho=k_{pp}} = -(k_{pp} h^2 / u) [-u \sin(u)/v + v \cos(u) + \cos(u) - u \sin(u)]$$

For the G_V case, the derivation of the residues is similar. However, the expression is a bit more complicated, since it has both TE and TM waves.

TABLE 2
Number of Modes and Number of Integration Points Needed at Different Distance Ranges for $h = \lambda$

Distance of ρ (in Terms of λ)	N_s (TE)	N_s (TM)	N_L (TE)	N_L (TM)	N_x (TE)	N_x (TM)	N_I (G_A)	N_I (G_V)
0.05	3	4	93	93	159	161	48	28
0.2	3	4	21	21	39	41	18	16
0.5	3	4	7	7	17	19	10	12
1	3	4	3	3	9	11	10	10
3	3	4	1	1	3	5	8	8
10	3	4	1	1	2	1	6	8

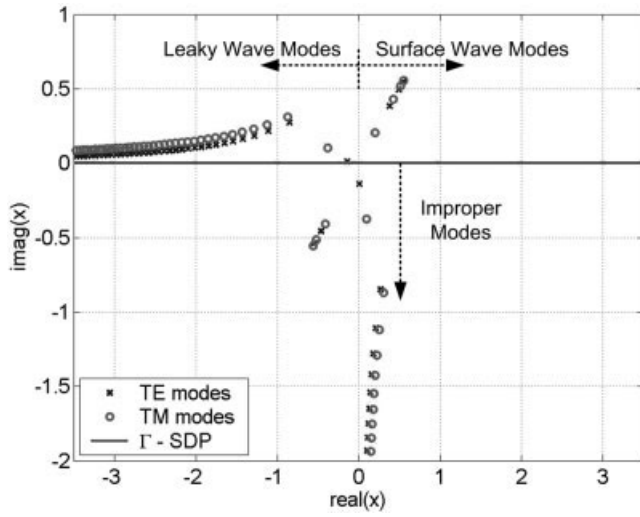


Figure 3 SDP and modes on the complex x plane for $h = \lambda$ and $\rho = 0.05 \lambda$

$$N(k_{pp}) = (k_0^2 v^2 \epsilon_1 / \epsilon_0 + k_0^2 u^2) \sin(2u) - 2k_0^2 v u \sin^2(u)$$

$$\begin{aligned} [dD(k_p)/dk_p]_{k_p=k_{pp}} = & j(k_p h v) \left[\left(\frac{v}{u} - \frac{u}{v} \right) \left(\frac{\epsilon_1}{\epsilon_0} \cos^2 u - \sin^2 u \right) \right. \\ & \left. + \cos 2u \left(\frac{\epsilon_1 v^2}{\epsilon_0 u} - u \right) - \sin 2u \left(\frac{\epsilon_1}{\epsilon_0} + 1 \right) (v + 1) \right]_{k_p=k_{pp}} \end{aligned}$$

In Figure 2, we can find that the leaky wave modes are close to Γ and are located gradually away from the saddle point ($\theta = \pi/2$ and $k_p = k_0$). On the other hand, the major component of the residues, the Hankel function, decays exponentially with the input valuable $k_{pp}\rho$. Therefore, we can use $\text{Im}(k_{pp})\rho \leq N_b$ to economically determine the number of leaky wave modes with lower mode index in order to speed up the calculation of the residues (Table 2 column 4 and 5).

To facilitate the integration along Γ , we can further map the complex k_p plane to the complex x plane by $k_p = k_0 - jx^2/(2\rho)$. The mapping relationship between x and θ is

$$x = 2\exp(-j\pi/4) \sqrt{\rho k_0} \sin(\theta/2 - \pi/4) \quad (16)$$

On the complex x plane, the SDP is along the real x axis from $-\infty$ to $+\infty$ (see Fig. 3). The integrand decreases from the saddle point ($x = 0$) in a Gaussian manner. Thus, we can transform the G_A^Γ by the following expression.

$$G_A^\Gamma = -\frac{j\mu_0}{8\pi} \int_{-\infty}^{\infty} dx \Phi_A(x) \exp\left(-\frac{x^2}{2}\right) \quad (17)$$

where

$$\Phi_A(x) = \frac{x}{\rho} \exp\left(\frac{x^2}{2}\right) \left(\frac{2k_p}{jk_0z + k_{1z} \cot(k_{1z}h)} \right) H_0^{(2)}(k_p \rho)$$

We can also use same transformation method to get the expression of $\Phi_V(x)$ for G_V^Γ .

$$G_V^\Gamma = -\frac{j}{8\pi\epsilon_0} \int_{-\infty}^{\infty} dx \Phi_V(x) \exp\left(-\frac{x^2}{2}\right) \quad (18)$$

where

$$\begin{aligned} \Phi_V(x) = & -j \frac{x}{\rho} \exp\left(\frac{x^2}{2}\right) \\ & \times \left[\frac{(k_0^2 v^2 \epsilon_1 / \epsilon_0 + k_0^2 u^2) \cot u - 2vuk_p^2}{k_0z k_p (v + u \cot u) ((\epsilon_1 / \epsilon_0) v \cot u - u)} \right] H_0^{(2)}(k_p \rho) \end{aligned}$$

When numerically integrating along the real x axis, some modes can be very close to the saddle point. Those modes will cause significant oscillations on the integrand. To smooth the integrand over the range between $-x_{\max}$ and x_{\max} , we adopt the NMSP method with poles extraction, which is presented in our previous paper [4]. The NMSP method can extract all the poles close to the saddle point, including not only proper modes but also improper modes.

For a pole θ_p , we can get the x_p location on the x plane by Eq. (16). In Figure 3, we plot the pole locations for $\rho = 0.05 \lambda$ and $h = 1$ wavelength in the complex x plane. We use $x_{\max} = 5$ and $N_b = 15$ in this article.

The closer the pole is to the saddle point in the complex x plane, the stronger the pole contributes to the oscillation of the integrand. The distance between pole and saddle point in the complex x plane is proportional to $\sqrt{k_0 \rho}$. Therefore, when ρ increases, we can efficiently count less number of poles for extraction calculation. In Table 2 column 6 and 7, we list the number of poles N_X that are extracted in NMSP.

Note that we only use less than 50 trapezoidal integration points for the SDP integration (Table 2 column 8 and 9), since we have also extracted the improper modes, which do not contribute as residues but have great effect on the oscillations of the SDP integrand. Figure 4 shows an illustration of the large difference between the G_V integrand over SDP before and after extraction of the poles.

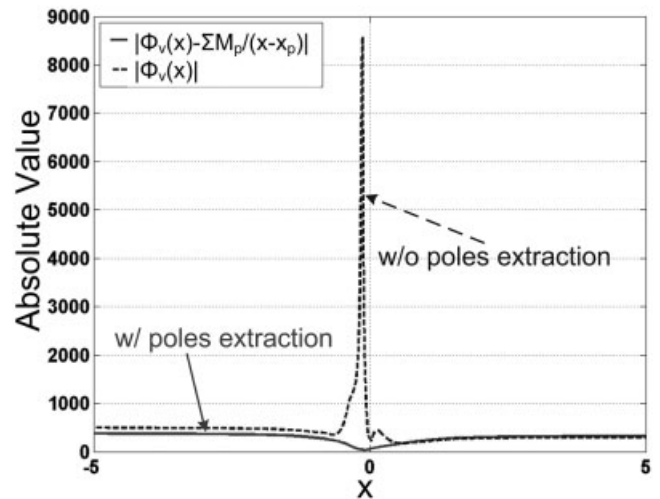


Figure 4 Illustration of the large difference between the G_V integrands before and after extraction of the poles for the case where $\rho = 0.05 \lambda$ and $h = \lambda$

2.4 Modified Half Space Extraction Method for Near Field $\rho < 0.05 \lambda$

In the half-space extraction method [11], we have

$$R^{\text{TM}} = (R^{\text{TM}} - R_{01}^{\text{TM}}) + R_{01}^{\text{TM}}$$

$$R^{\text{TE}} = (R^{\text{TE}} - R_{01}^{\text{TE}}) + R_{01}^{\text{TE}}$$

R_{01}^{TM} and R_{01}^{TE} represents the half-space solution, $R^{\text{TM}} - R_{01}^{\text{TM}}$ and $R^{\text{TE}} - R_{01}^{\text{TE}}$ represents the remainder after half-space extraction.

Thus,

$$G_A = G_A^{(N)} + G_A^{(H)}$$

$$G_V = G_V^{(N)} + G_V^{(H)}$$

where (N) denotes the numerical evaluation of the remainder along the SIP and (H) denotes the half-space portion evaluated by using two vertical branch cuts associated with k_0 and k_1 , respectively. The detailed expressions can be found in [12]. There is no pole associated with R_{01}^{TM} and R_{01}^{TE} in the upper Riemann sheet if vertical branch cuts are used [7]. We use Gauss-Hermite quadratures for the integrations along the vertical branch cuts, since the integrands decay in a Gaussian manner and are smooth. In the near field, we found the contributions from the remainder are fairly constant and only account for 1% of the total magnitude. Therefore we only invoke numerical evaluation of the remainder along the SIP once as the pre-processing for all distances in the near field region.

NUMERICAL RESULTS

In Table 2, we list:

- N_S = number of surface wave modes excited,
- N_L = number of leaky wave modes needed for $\text{Im}(k_{pp}) \rho \leq 15$,
- N_X = number poles extracted for the Γ integration for $x_0 \leq 5$,
- N_I = number of trapezoidal integration points in the numerical integration, for various distances for the case where $h = 1$ wavelength.

Table 2 shows that as ρ increases, we need fewer points for poles extraction, fewer points for integration and fewer points for residue calculation. Therefore the NMSP method requires less time to evaluate as ρ gets larger.

Table 3 shows the CPU run time for computing G_A and G_V due to a HED in layered media for $h = 1$ wavelength on all ranges of ρ . All times were taken on a Pentium IV 3.2 GHz PC running Matlab. The FAM/NMSP methods can compute layered medium Green's functions for the range $0.05\lambda \leq \rho \leq \infty$. The pre-processing CPU is 0.34 s for computing the locations of 500 modes. Once the exact locations of all modes are determined, including surface wave modes, leaky wave modes and improper modes, we can rapidly evaluate the layered medium Green's function by fully exploiting the different types of poles according to their locations. For

TABLE 3
CPU Run Time Per Point for All Distance Ranges for G_A and G_V

Range of ρ	CPU for G_A ($h = \lambda$)	CPU for G_V ($h = \lambda$)
$\rho < 0.05\lambda$	0.543ms	0.785ms
$0.05\lambda < \rho < 0.2\lambda$	4.110ms	5.422ms
$0.2\lambda < \rho < 2\lambda$	1.906ms	2.359ms
$\rho > 2\lambda$	1.469ms	1.798ms

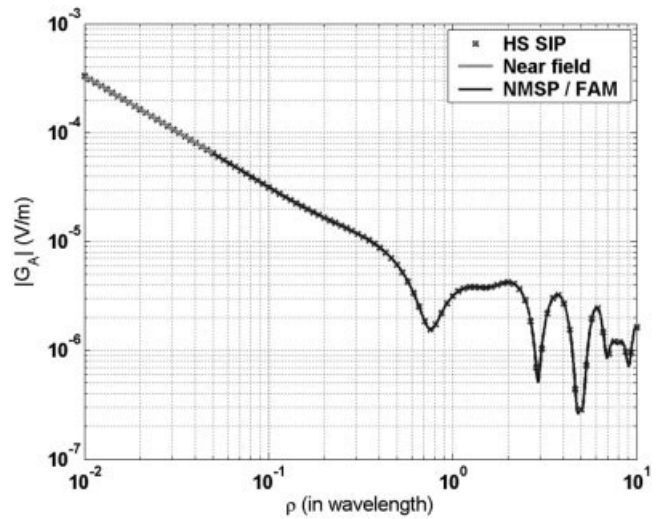


Figure 5 $|G_A|$ as a function of ρ due to a HED in single layered media for $h = \lambda$

example, surface wave poles and leaky wave poles contribute to the calculation of the residues, which is independent from the space coordinate dependent factor $H_0^{(2)}(k_{pp}\rho)$ for all field points. All the proper and improper poles that are close to saddle point need to be extracted and replaced by error functions for the NMSP implementation. After pre-processing, the CPU per distance point in Table 3 covers the rest of the computation, which consists of the summation of the $N_S + N_L$ residues, the computation of the N_X incomplete error functions and the N_I trapezoidal integration points. The CPU per point is of the order of 1–5 ms. Thus, for instance, to compute the fields at 1000 arbitrary distance points that can be at all distance ranges, the total CPU is $0.34 + 1000 \times 0.003 = 3.34$ s. Note that for the very near field of $\rho < 0.05\lambda$, we use the modified half space extraction method with Gauss-Hermite integration along the vertical branch cuts. For the G_A case, we use 22 Gauss-Hermite quadratures; for the G_V case, we use 56 Gauss-Hermite quadratures when integrating along the vertical branch cuts. Figure 5 shows G_A and Figure 6 shows G_V , the magnitudes of the spatial domain layered medium Green's functions for mixed potentials due to a HED as a function of the horizontal

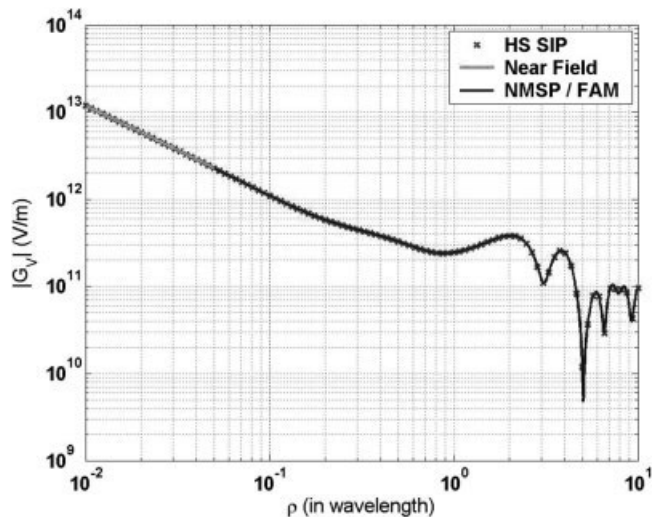


Figure 6 $|G_V|$ as a function of ρ due to a HED in single layered media for $h = \lambda$

distance ρ for $0.01\lambda < \rho < 10\lambda$, where $\epsilon_r = 4$, $\mu_r = 4$ and $h = 1$ wavelength. The solid line is the result using our FAM/NMSP based fast method and the cross-dotted line is the result using the conventional half space extraction method. The comparison confirms the accuracy of the FAM/NMSP method to within 0.2%. These highly matched results prove that our FAM method can determine all the pole locations precisely. This method can be extended to treat multi-layered, lossy dielectric/conductor, ferrite and optical media as well.

REFERENCES

1. Y.L. Chow, J.J. Yang, D.G. Fang, and G.E. Howard, A closed-form spatial Green's function for the thick microstrip substrate, *IEEE Trans Microwave Theory Tech* 39 (1991), 588–592.
2. M. Yuan, T.K. Sarkar, and M. Salazar-Palma, A direct discrete complex image method from the closed-form Green's functions in multilayered media, *IEEE Trans Microwave Theory Tech* 43 (2006), 1025–1032.
3. L. Tsang, C.-J. Ong, and B. Wu, Electromagnetic fields of Hertzian dipoles in thin-layered media, *IEEE Antennas Wireless Propag Lett* 5 (2006), 537–540.
4. L. Tsang and B. Wu, Electromagnetic fields of Hertzian dipoles in layered media of moderate thickness including the effects of all modes, *IEEE Antennas Wireless Propag Lett*, in press.
5. M. Guglielmi and D.R. Jackson, Low-frequency location of the leaky-wave poles for a dielectric layer, *IEEE Trans Microwave Theory Tech* 38 (1990), 1743–1746.
6. C.-I.G. Hsu, R.F. Harrington, J.R. Mautz, and T.K. Sarkar, On the location of leaky wave poles for a grounded dielectric slab, *IEEE Trans Microwave Theory Tech* 39 (1991), 346–349.
7. M.A. Marin, S. Barkeshli, and P.H. Pathak, On the location of proper and improper surface wave poles for the grounded dielectric slab, *IEEE Trans Antennas Propag* 38 (1990), 570–573.
8. M.J. Neve and R. Paknys, A technique for approximating the location of surface- and leaky-wave poles for a lossy dielectric slab, *IEEE Trans Antennas Propag* 54 (2006), 115–120.
9. Y. Wang, B.L. Ooi and M.S. Leong, An efficient and fast approach for surface-wave pole extraction in two-layered microstrip geometry, *Microwave Opt Technol Lett* 41 (2004), 253–258.
10. J.A.C. Weideman, Computation of the complex error function, *SIAM J. Numer Anal* 31 (1994), 1497–1518. <http://dip.sun.ac.za/~weideman/research/cef.html>
11. L. Tsang, C.-C. Huang, and C.H. Chan, Surface electric fields and impedance matrix elements of stratified media, *IEEE Trans Antennas Propag* 48 (2000), 1533–1543.
12. L. Tsang, C.-J. Ong, C.-C. Huang, and V. Jandhyala, Evaluation of the Green's function for the mixed potential integral equation (MPIE) method in the time domain for layered media, *IEEE Trans Antennas Propag* 51 (2003), 1559–1571.

© 2007 Wiley Periodicals, Inc.

A STEERABLE ARRAY ANTENNA USING CONTROLLABLE 4-BIT DIELECTRIC SLAB PHASE SHIFTERS ON A COPLANAR WAVEGUIDE AT 24 GHz

Junho Cha and Yasuo Kuga

Department of Electrical Engineering, University of Washington, Box 352500, Seattle, WA 98195; Corresponding author: junho2@u.washington.edu

Received 10 May 2007

ABSTRACT: A steerable antenna using a movable dielectric phase shifter is designed and developed. The change of the effective dielectric constant at different dielectric slab positions on a CPW is used as the

phase shifter. The impedance matching and desired phase shift conditions are satisfied at two slab heights. Additionally, the reflection is designed to be minimized at these slab positions and at the designed frequency. A low-loss dielectric material is used as the dielectric slab and is placed close to a coplanar transmission line with an airgap. A tapered 8×7 steerable array antenna with phase shifters is designed and fabricated at 24 GHz. The *E*- and *H*-plane radiation patterns are measured at different phase shift positions and compared with the expected results. © 2007 Wiley Periodicals, Inc. *Microwave Opt Technol Lett* 49: 3118–3122, 2007; Published online in Wiley InterScience (www.interscience.wiley.com). DOI 10.1002/mop.22906

Key words: coplanar waveguide; phase shifter; steerable array antenna

1. INTRODUCTION

Phase shifters are a critical element for electronically scanning phased-array antennas, and typically account for a significant amount of the cost of producing an antenna array. The reduction of fabrication cost opens exciting possibilities for many applications. Recently, different types of microwave phase shifters, including those that are MEMS-based and ferroelectric-based, have been proposed for antenna applications [1]. Additionally, phase shifters using a PZT controlled dielectric layer to perturb the electromagnetic fields of a CPW have been demonstrated [2].

In our previous studies, we have demonstrated that a movable dielectric slab which is placed close to a CPW with an airgap can be used as a phase shifter for an array antenna [3–5]. This array antenna consists of series-fed patch antennas, phase shifters, and a feeding network, as shown in Figure 1. For our design purposes, the best dielectric materials seem to be in the range of $\epsilon_r \approx 3$ to 10. Because we are introducing the impedance mismatch section on the TL, the elimination of reflection is essential to the design of the phase shifter. Also, we explore possible solutions for the impedance mismatch problems [4, 5]. To minimize the reflection caused by the dielectric slab and also to obtain the desired phase shifter, the dielectric constant of the slab has to be set to a specific value.

In this letter, we present a steerable array antenna with a 4-bit phase shifter designed at 24 GHz unlicensed band. The initial design which is shown in Figure 1(a) has a large side-lobe in the *E*-plane due to the interference from the CPW and the feeding network. To mitigate it, we placed both the CPW and the feeding network section on the bottom side as shown in Figure 1(b). By using a 4-bit phase shifter, the antenna beam angle can be scanned from -52.5° to $+52.5^\circ$.

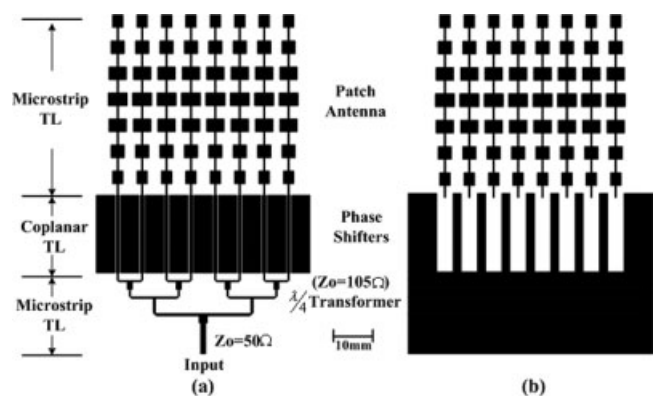


Figure 1 Block diagram of an 8×7 steerable array antenna. (a) Front feeding, (b) back feeding